Ionics (2022) 28:5609–5621
https://doi.org/10.1007/s11581-022-04766-2

ORIGINAL PAPER

Preparation of $ZnCo_2O_4$ nanowire arrays with high capacitive by a one-step low-temperature water bath and calcination methods

Jing Wang[1] · Gang Wang[1] · Jian Hao[2] · Xiang Zhang[3]

Received: 21 May 2022 / Revised: 6 September 2022 / Accepted: 19 September 2022 / Published online: 26 September 2022

Abstract

In this paper, $ZnCo_2O_4$ nanowire arrays (NWAs) were successfully prepared on carbon cloth (CC) conductive substrates using a water bath method followed by calcination treatment. The as-prepared $ZnCo_2O_4$ NWAs were uniformly grown on the conductive substrates and their length was about 10 um. Cyclic voltammetry, charge–discharge, and the other electrochemical testing methods were used to research the electrochemical performance of the $ZnCo_2O_4$ NWAs. The results indicate that the product had a good specific capacity and cyclic stability. When the current density is 1 A g^{-1}, the specific capacity of the as-prepared $ZnCo_2O_4$ NWAs reaches 2300 F g^{-1}. The cycling stability of the $ZnCo_2O_4$ NWAs reaches 96.84% after 10,000 cycles at a current density of 5 A g^{-1}. In addition, we have assembled an asymmetric supercapacitor by using the material and activated carbon (AC) as positive and negative electrodes, respectively. The device has a maximum voltage window of 1.6 V and can operate in this voltage range class. The device has a good specific capacity (248 F g^{-1} at 1 A g^{-1}) and excellent capacity retention (97.42% after 10,000 cycles at 5 A g^{-1}). The relevant experimental data show that it has a maximum energy density of 88.18 Wh kg^{-1} (specific power of 800 W kg^{-1}) and a maximum power density of 12,000 W kg^{-1} (specific energy of 53.69 Wh kg^{-1}). In this paper, $ZnCo_2O_4$ nanowire materials were prepared by water bath and calcination, which provided a strategy for preparing high-performance electrode materials.

Keywords $ZnCo_2O_4$ · Supercapacitor · Nanowire arrays · Electrode material · Flexible energy storage device

Introduction

With the development of science and technology and the needs for human production and life, the problems of environmental pollution and energy scarcity have gradually intensified. Currently, storing energy mainly relies on batteries. But the batteries usually contain environmentally unfriendly materials (lithium, lead-acid, etc.). There are urgent needs for efficient storage performance, low-cost, and green energy storage devices. With high power density, fast charging and discharging, green environment protection, and long service life, supercapacitors are considered one of the most promising energy storage devices among the new energy storage technologies in the energy fields [1–5]. However, the energy density of supercapacitor is relatively low, which greatly affects their application in the market [6–8]. According to the energy density equation $E = 1/2CV^2$, energy density is directly related to the specific capacitance (C_S) and voltage window (V) [9–11]. By designing and developing electrode materials with excellent properties, the specific capacitance can be improved [12]. In addition, by using two different electrode materials and assembling asymmetric supercapacitors, the voltage window can be expanded and thus the energy density can be improved [13]. Therefore, the exploration of high-performance electrode materials has become a research hotspot worldwide. Compared to the conventional carbon materials, multi-metal oxides are not only environmentally friendly and stable in nature, but also have significant synergistic effects and rich microstructures. These advantages are useful to increase the electrical conductivity, specific surface area, surface active sites, and

✉ Jing Wang
wangwangmayong@126.com

[1] School of Light Industry, Harbin University of Commerce, Harbin 150028, People's Republic of China

[2] State Key Laboratory of High-Efficiency Utilization of Coal and Green Chemical Engineering, Ningxia University, Yinchuan, Ningxia 750021, People's Republic of China

[3] Center for Composite Materials and Structure, Harbin Institute of Technology, Harbin 150001, People's Republic of China

other favorable factors, all of which effectively enhance the electrochemical properties of the materials [14–16]. Wang et al. [17] reported multilayer $CoFe_2O_4$ hollow microspheres with a high specific capacitance value of 1231 F g^{-1}. Han et al. [18] reported a specific capacitance of 810.93 F g^{-1} for $SrBiO_3$ at a current density of 1 A g^{-1}. Guan et al. [19] reported that the specific capacitance of $NiCo_2O_4$ nanocomposite materials was 1055.3 F g^{-1}. Among these bimetallic oxides, $ZnCo_2O_4$ [20] has a unique pore size structure, large specific surface area, good electrical conductivity, and large theoretical specific capacity, which makes it a very promising electrode active material for supercapacitors. Zhu et al. [21] successfully prepared the porous $ZnCo_2O_4$ nanosheets. The capacitance maintenance rate reached 96.3% after 5000 cycles of charge and discharge, indicating an excellent cycling stability performance. Shang et al. [22] prepared hollow $ZnCo_2O_4$ nano-microspheres. The material had a high specific capacitance of 776.2 F g^{-1}. Xu et al. [23] prepared porous $ZnCo_2O_4$ nanostructured materials. The $ZnCo_2O_4$// RGO asymmetric devices exhibited a high energy density of 84.48 Wh kg^{-1} at a wide potential window of 1.6 V. Therefore, the design and development of electrode materials with excellent electrochemical properties are an important strategy to drive the commercialization of supercapacitors.

Among the many preparation methods, the nanostructured materials synthesized by the water bath method can be grown directly onto the conductive substrate, the active material can be uniformly distributed on its surface, and the substrate structure can remain stable with good bonding between the active material. Calcination treatment has many advantages. Firstly, it can keep the matrix structure stable and combine well with the active material. Secondly, it can also eliminate any bad impurities produced in the early preparation to ensure uniform and stable metal dispersion on the carrier. Therefore, in this paper, the precursors were first prepared in a water bath, and then the electrochemical properties of the materials were improved by calcination treatment.

In this paper, $ZnCo_2O_4$ NWAs were successfully prepared using a simple one-step water bath method and calcination treatment. These nanowires grow interlaced with each other and formed large number of pores structures. These characteristic advantages facilitate the transfer of ions and electrons between the material interface and surface. The $ZnCo_2O_4$ electrode has a high specific capacitance of 2300 F g^{-1} at a current density of 1 A g^{-1} and a capacitance retention rate of 96.84% with good cycling stability. At last, we assembled the asymmetric supercapacitor device using the as-prepared $ZnCo_2O_4$ NWAs as the positive electrode and the AC as the negative electrode. This asymmetric device shows a wide potential window of 1.6 V, a high energy density of 88.18 Wh kg^{-1} (the power density of 800 W kg^{-1}), and excellent cycling performance (97.42% after 10,000 charge/discharge cycles).

Experiment

As a conductive substrate, CC has good electrical conductivity and a loose fiber braided structure, which is conducive to the diffusion of electrolytes into the electrode material. At the same time, the specific capacity of CC is low and its properties are stable. Therefore, its electrochemical performance analysis of materials can be almost ignored. In the experiments, analytical grade reagents were used without further purification.

Preparation of $ZnCo_2O_4$ NWAs electrodes

CC as a conductive substrate has good electrical conductivity and a loose fiber weave structure, and this structure facilitates the full diffusion of electrolytes into the electrode material. In this paper, $ZnCo_2O_4$ NWAs were prepared on the surface of CC as a conductive substrate using a one-step water bath thermal method followed by heat treatment. The $ZnCo_2O_4$ NWAs were prepared directly grown on CC by one-pot low-temperature water bath method with the reaction temperature of 80 ℃ for 2 h. Firstly, 1 mmol $Zn(NO_3)_2 \bullet 6H_2O$, 3 mmol $Co(NO_3)_2 \bullet 6H_2O$, 3.5 mmol $CO(NH_2)_2$, and 2 mmol NH_4F were mixed in 40 ml of ultrapure water with sonication for 3.5 h. The mixtures were placed in a water bath with a piece of cleaned CC and kept at 80 ℃ for 3 h. Then, the samples were cooled to room temperature and dried for 8 h in an oven at 50 ℃. Then, the samples were calcined at 550 ℃ for 5 h. Finally, $ZnCo_2O_4$ NWAs electrode was obtained.

Preparation of AC electrode

AC material was used as the negative electrode material for the asymmetric device. The preparation process of this negative electrode material is as follows: the corresponding proportions of activated carbon, carbon black, and polyvinylidene fluoride (PVDF) (mass ratio $R = 85:10:5$) are firstly weighed, and the weighed powder is ground in a mortar. Then, the well-ground powder is added to an appropriate amount of N-methyl-pyrrolidone (NMP) organic solvent. Finally, the above mixture was stirred on a magnetic stirrer for a certain time until a homogeneous and viscous slurry was formed. The slurry is evenly applied to a CC conductive substrate with an area of 1×1 cm^2. The treated activated carbon negative electrode material was put into a vacuum drying oven and dried at 60 ℃ for 6 h. The AC electrode was successfully prepared.

Preparation of gel state asymmetric supercapacitor

An asymmetric supercapacitor device was assembled using the $ZnCo_2O_4$ electrode as the positive electrode and the activated carbon electrode as the negative electrode. The PVA/KOH gel electrolyte was synthesized by adding 2.8 g KOH and 3 g polyvinyl alcohol (PVA) to 25 mL deionized water. The electrode materials and separators were immersed in the PVA/KOH gel electrolyte for a few minutes by heating and stirring at 80 °C for 5 h. The electrode materials were then removed from the gel and the separators were immersed in the PVA/KOH gel electrolyte. Then, they were removed from the gel electrolyte and assembled together. The device was placed in the air for 12 h and became solid.

Electrochemical performance test

The electrochemical performance tests in this thesis were carried out using the Shanghai C&H CHI660C electrochemical workstation. The tests under three-electrode conditions were carried out with a 1×4 cm^2 platinum sheet as the counter electrode and the test electrolyte was an alkaline 2 M KOH solution, so a saturated glycerol electrode was chosen as the reference electrode for the tests in the experiment, and the prepared material was used directly as the working electrode to test the capacitive performance. The device's electrochemical properties were tested under two-electrode conditions and the rest of the conditions were identical. Cyclic voltammetry (CV), constant current charge/discharge (GCD), and electrochemical impedance spectroscopy (EIS, 0.01 ~ 100 kHz with an amplitude of 5 mV) were tested, and the calculated capacitance was as follows:

$$C_s = It/mV \tag{1}$$

C_S (F g^{-1}) is the specific capacitance of a single electrode. I (A) represents the discharge current. Δt (s) is the discharge time. m (g) is the mass of the active material, and ΔV (V) is the voltage window. The electrochemical measurements of the energy density (E) and power density (P) of the device are calculated by the following equations. Herein, the mass of positive $ZnCo_2O_4$ is 2.5 g, and the mass of activated carbon AC is 0.32 g calculated according to Eq. 3.

$$q = C \times \Delta V \times m \tag{2}$$

$$m_+/m_- = \left(C_- \times \Delta V-\right)/\left(C_+ \times \Delta V_+\right) \tag{3}$$

$$E = O.5C_S V^2 \tag{4}$$

$$P = 3600E/t \tag{5}$$

Material characterization

The morphology of the prepared samples was observed with a scanning electron microscope (SEM, JEOL JSM-7500F) and a transmission electron microscope (TEM, JEOL JEM-2100F). The crystal structure of the prepared materials was observed by X-ray diffraction (XRD, RigakuD/max-2600 PC, radiation source Cu Kα, $\lambda = 1.5406$ Å). Electrochemical tests were carried out on a Shanghai Chenhua CHI660E electrochemical workstation.

Results and discussion

The morphological tests of the as-prepared samples are shown in Fig. 1. Figure 1 a shows the SEM image of the CC, which can be found to be composed of many carbon fibers with a single carbon-fiber diameter of 10 μm. Figure 1b shows the SEM images of $ZnCo_2O_4$ nanowires on the CC conductive substrate. It can be clearly seen that a large number of $ZnCo_2O_4$ NWAs are uniformly distributed on the CC conductive substrate skeleton. Figure 1c shows a high magnification SEM image of $ZnCo_2O_4$ NWAs and it can be found that the nanowires are of uniform size. $ZnCo_2O_4$ NWAs are interconnected to form a structure and this structure increases the specific surface area of the material, which can make the electrons and ions fully react with the active material more adequately and thus store more charges. In order to further analyze the elemental composition of the products, we performed SEM mapping tests on the products, as shown in Fig. 1d. The results show the presence of three elements, Zn, Co, and O, and no other elements, indicating that the prepared product is pure $ZnCo_2O_4$.

To further investigate the nanostructure of $ZnCo_2O_4$, we performed TEM tests on the products. As can be seen from Fig. 2a, the diameter of a single nanowire is 20 nm. Figure 2b is an HRTEM image of the product. It can be found that the lattice spacing of the prepared $ZnCo_2O_4$ is 0.23 nm and 0.24 nm, respectively. The results were corresponding to the (222) and (311) lattice planes of $ZnCo_2O_4$. TEM mapping test is carried out in the yellow box in Fig. 2a in the illustration. It can be found that there are only three elements of Zn, Co, and O. Figure 2c shows the EDS test of the product with CC as the conductive substrate, the results show the presence of Zn, Co, O, and C elements. This was consistent with the EDS and TEM results, indicating that the prepared samples were $ZnCo_2O_4$. Figure 2d shows the XRD pattern of the material, showing $ZnCo_2O_4$ as a crystalline structure, which is confirmed as $ZnCo_2O_4$ (JCPDS Card No. 23–1390) and the peak intensity is also high without the presence of other impurity peaks. The above multiple results indicate that the prepared sample is $ZnCo_2O_4$ with high purity.

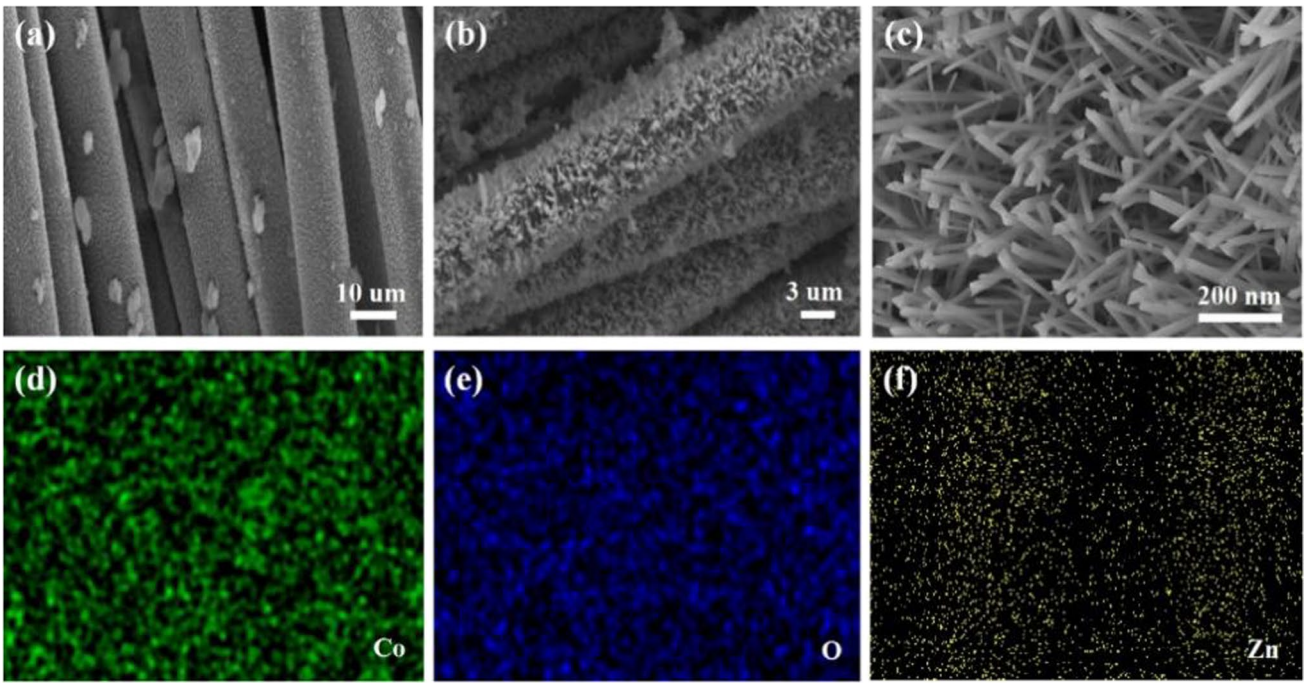

Fig. 1 **a–c** SEM images of $ZnCo_2O_4$ nanowires at different magnifications; **d–f** elemental mapping by EDS of Co, O, and Zn elements, respectively]

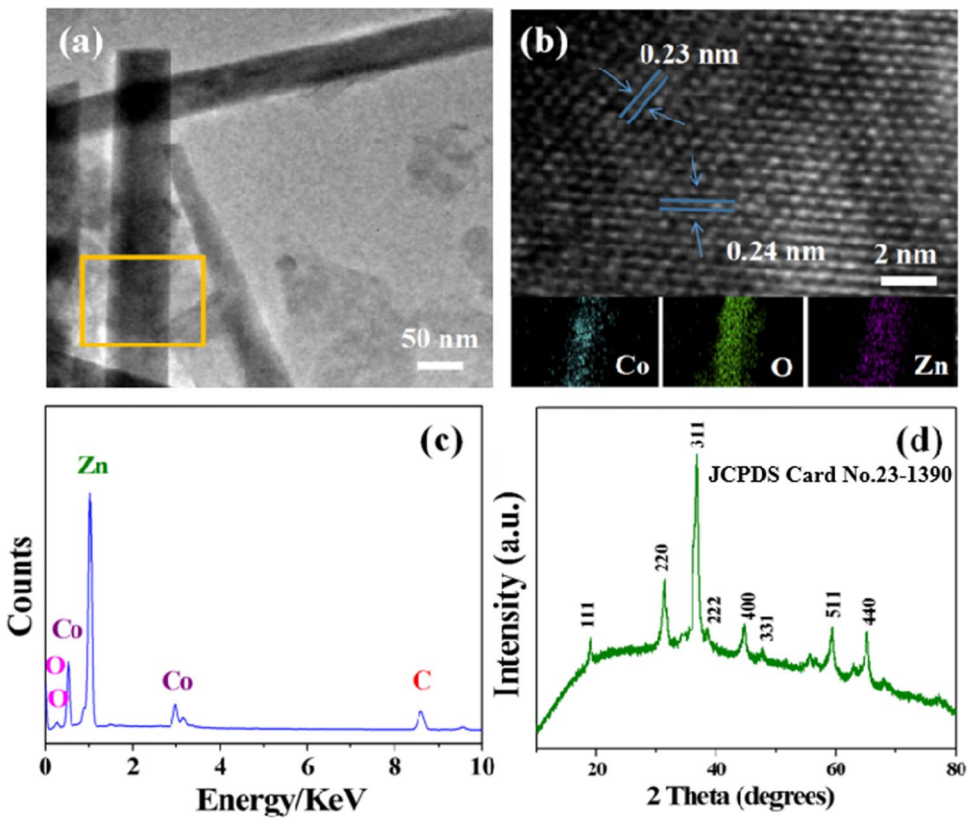

Fig. 2 **a** TEM image of $ZnCo_2O_4$ NWAs structure. The area in the orange box is used for the HRTEM test of $ZnCo_2O_4$ NWAs structure; **b** HRTEM images of $ZnCo_2O_4$ NWAs structure; **c** EDS measurement of $ZnCo_2O_4$ NWAs; **d** XRD patterns of $ZnCo_2O_4$ NWAs materials

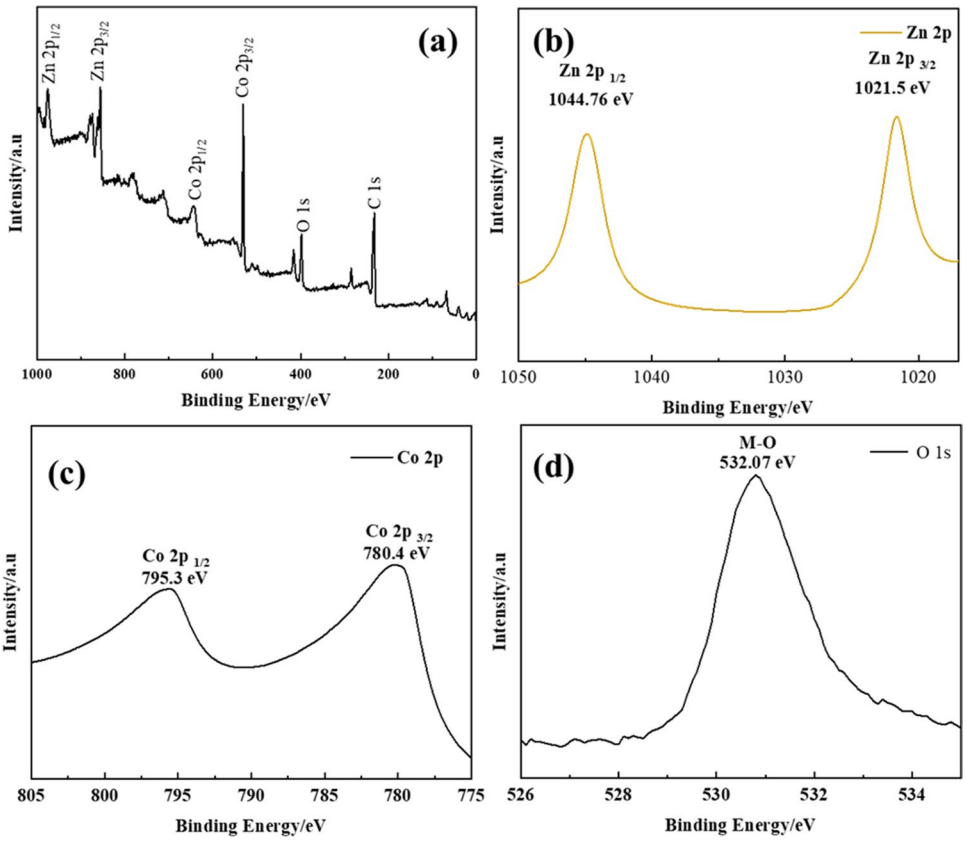

Fig. 3 XPS of $ZnCo_2O_4$: **a** survey scan, **b** Zn 2p, **c** Co 2p, and **d** O 1 s

We also further studied the surface chemical composition and elemental composition of the obtained samples. XPS test method was used to characterize and analyze the samples, as shown in Fig. 3a. Through XPS analysis of the composite, we can find that peaks of four elements, O, C, Zn, and Co, exist simultaneously in the total spectrum. Among them, C is from CC, while Zn, Co, and O are from zinc cobaltate, and no peaks of other elements are found, which is consistent with the XRD test results. In the peak spectrum of C, the peak of carbon is located at 248.8 eV, which is the standard peak spectrum of carbon [24, 25]. Figure 3b shows the XPS diffraction peak spectrum of Zn 2p, where Zn $2p^{1/2}$ is located at the peak position of 1044.76 eV, while Zn $2p^{3/2}$ is located at the peak position of 1021.5 eV, and the difference between the two peaks is about 23.23 eV, representing the Zn $2p^{1/2}$ and Zn $2p^{3/2}$ peaks of Zn^{2+}, respectively [26]. Figure 3c shows the energy spectrum of Co 2p, with two sharp peaks observed at 795.3 eV and 780.4 eV, corresponding to Co $2p^{1/2}$ and Co $2p^{3/2}$, respectively, with a difference of about 14.9 eV between the two peak positions [27]. The peak spectrum of O 1 s is shown in Fig. 3d, in which the peak at 532.07 eV is a typical metal–oxygen bond, while the peak at 530 eV is an oxygen ion bond with low coordination between metal and surface. The difference between the two peaks is about 2.07 eV, which is consistent with the values reported in previous literature [28]. The above peak values are consistent with the theoretical values of zinc ions occupying tetrahedral positions in spinel structures. The above analysis shows that the oxidation valence states of Zn (II) and Co (III) are consistent with the corresponding valence states of $ZnCo_2O_4$. XRD and XPS results show that the samples are high-purity $ZnCo_2O_4$.

In the paper, we also analyzed the formation mechanism of $ZnCo_2O_4$ nanowires [29]. In the initial stage of the water bath thermal reaction, the Zn^{2+} ions and $Co_2O_4^{2-}$ ions dissolved in the solution combine to form small $ZnCo_2O_4$ nuclei particles, which are aggregated on the CC. These nanoparticles are unstable due to their large surface energy. As the reaction proceeds, these small nanoparticles will continue to aggregate and become larger thus reducing the surface energy. By controlling the reaction time and temperature of the water bath thermal reaction, the $ZnCo_2O_4$ nanowire structure can be formed by directional growth.

In the experiment, the electrochemical performances of $ZnCo_2O_4$ NWAs were tested in a three-electrode system using 2 M KOH as an electrolyte. At a sweep rate of 5 mV s^{-1}, we plotted the cyclic voltammetric curves of CC and $ZnCo_2O_4$ NWAs, as shown in Fig. 4a. The results show that the specific capacity of the $ZnCo_2O_4$ NWAs electrode is much higher than that of the pure CC, indicating that the contribution of pure CC to the capacitance of the $ZnCo_2O_4$ NWAs electrode is negligible. Figure 4b shows the constant

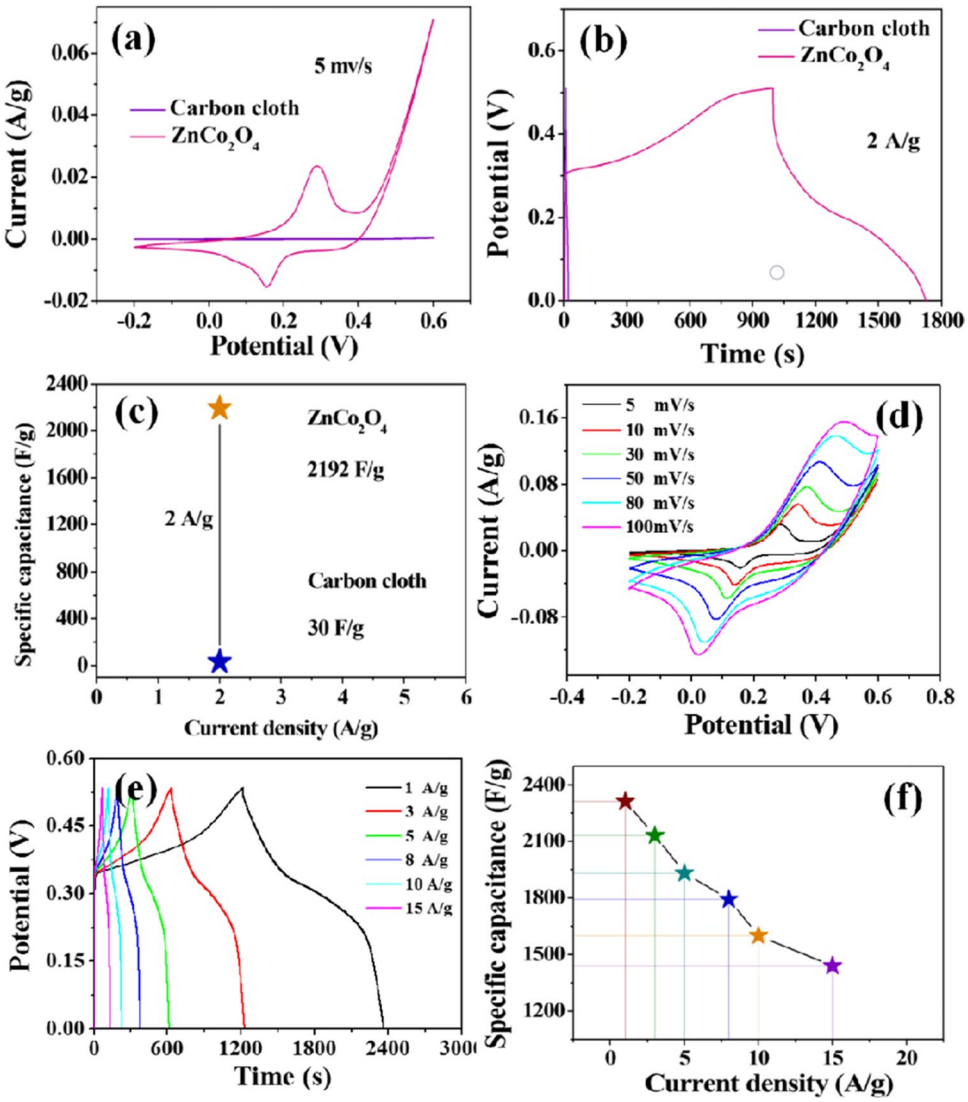

Fig. 4 **a** Cyclic voltammetry curves of CC, $ZnCo_2O_4$ NWAs; **b** charge and discharge of CC and $ZnCo_2O_4$ NWAs at the current density of 2 A g^{-1}; **c** comparison of specific capacity between CC and $ZnCo_2O_4$ NWAs at 2 A g^{-1}; **d** cyclic voltammetry of $ZnCo_2O_4$ NWAs at different sweep rates; **e** charge and discharge tests of $ZnCo_2O_4$ NWAs under different current intensities; **f** specific capacitance diagram of $ZnCo_2O_4$ NWAs under different current densities

current charge–discharge curves of the CC and $ZnCo_2O_4$ NWAs electrodes. At a current density of 2 A g^{-1}, the discharge time of the $ZnCo_2O_4$ NWAs electrode is much longer than that of the CC electrode. It also shows that the specific capacity of the $ZnCo_2O_4$ NWAs electrode is much larger than that of the CC. From Eq. 1, we calculated the specific capacitance of the CC and $ZnCo_2O_4$ NWAs electrodes at a current density of 2 A g^{-1}, as shown in Fig. 4c. The specific capacitances of the CC and $ZnCo_2O_4$ NWAs were 30 F g^{-1} and 2192 F g^{-1}, respectively. These results further confirm that the CC has little effect on the total capacitance of the $ZnCo_2O_4$ NWAs electrode. Figure 4d shows the CV curves of the $ZnCo_2O_4$ NWAs electrode at different sweep rates. The CV curves show obvious redox peaks, which indicate that $ZnCo_2O_4$ NWAs are pseudocapacitive energy storage properties. As the scan rate increased, the peak current increased. The curve increases proportionally and the shape remains basically unchanged. It indicates that it has good electrochemical reversibility and the prepared $ZnCo_2O_4$ NWAs electrode has fast electron and ion transport capability. In addition, the charge storage mechanism of $ZnCo_2O_4$ NWs has also been investigated in this paper. Under alkaline conditions, Zn ions readily react with OH^- in solution to form $Zn(OH)_4^{2-}$. When the temperature gradually increases to a suitable temperature, Co^{2+} and Zn^{2+} react with hydroxyl ions to form $ZnCo_2(OH)_4$ particles. By contacting with air, the $ZnCo_2O_4$ microstructure is eventually formed [30]. The chemical reactions involved are as follows.

$$Zn^{2+} + 4OH^- \rightarrow Zn(OH)_4^{2-} \tag{6}$$

$$Zn(OH)_4^{2-} \rightarrow ZnO + H_2O + 2OH^- \tag{7}$$

$$2Co^{2+} + Zn^{2+} + 6O^{H^-} \rightarrow ZnCo_2(OH)_4 \tag{8}$$

$$ZnCo_2(OH)_4 + \frac{1}{6}0_2 \rightarrow ZnCo_2O_4 + 3H_2O \quad (9)$$

Figure 4e shows the constant current charge and discharge curves at different current densities. These charge/discharge curves have good symmetry and show good electrochemical reversibility. However, there is still a phenomenon of shorter discharge time, which is mainly due to the chemical charge storage in the whole process, and the ions and electrons will have certain influence in the embedding or ejection process [31]. The specific capacitance values of the $ZnCo_2O_4$ NWAs electrodes were calculated to be 2300, 2130, 1940, 1792, 1620, and 1440 F g^{-1} at current densities of 1, 3, 5, 8, 10, and 15 A g^{-1}, respectively, as shown in Fig. 4f. The theoretical specific capacity of $ZnCo_2O_4$ is 2604 F g^{-1}. At the current densities of 1, 3, 5, 8, 10, and 15 A g^{-1}, the specific capacity reaches 2300, 2130, 1940, 1792, 1620, and 1440 F g^{-1}, respectively. The ratio and capacity retention rates reached 88.3%, 81.8%, 74.6%, 68.8%, 62.2%, and 55.3%, respectively. Through the search of relevant literature, the multiplier performance is still very excellent [32–35]. The results indicate that the prepared $ZnCo_2O_4$ NWAs electrodes have excellent electrochemical properties.

In order to further investigate the diffusion effect of $ZnCo_2O_4$ nanomaterial, we tested the cyclic voltammetry curve of $ZnCo_2O_4$ nanomaterial under different scanning speeds and different conditions, and studied the kinetic behavior of $ZnCo_2O_4$ nanomaterial in detail. Figure 5a shows the CV curves of $ZnCo_2O_4$ NWAs materials at different sweeping speeds. It can be found that with the increase of sweeping speed, the CV curves of materials also gradually increase, which is due to the increase of the response current of materials due to the large sweeping speed. In addition, the oxidation peak shifts to the high voltage while the reduction peak shifts to the low voltage with the gradual increase of the sweeping speed, and the difference of polarization voltage increases [36]. According to the current research theory, the electrochemical properties of materials are mainly affected by the pseudocapacitance behavior controlled by diffusion and surface control. According to literature reports [37, 38], the electrochemical behavior of $ZnCo_2O_4$ NWAs can be analyzed by using the formula ($i = av^b$, $\log(i) = b\log(v) + \log(a)$, $i = k1v + k2v^{1/2}$). For a value of b close to 0.5, the performance is limited by the diffusion control behavior, while a value of b close to 1.0 indicates pseudocapacitance behavior, which is determined by capacitance. Figure 5b shows the contribution rate of pseudocapacitance capacity at different sweeping speeds. It can be found that the capacitance proportion gradually increases with the increase of sweeping speed. According to the phase of gradual reaction represented by the highest redox peak, the b values of cathode and anode processes are 0.68 and 0.58, respectively, as shown in Fig. 5c. It shows that the reaction of $ZnCo_2O_4$ NWAs is a mixed behavior [39]. According to the above formula, the capacitance contribution of $ZnCo_2O_4$ NWAs is 54.6% at 10 mV s^{-1}, and the ratio increases to 82.2% at 100 mV s^{-1}. These results

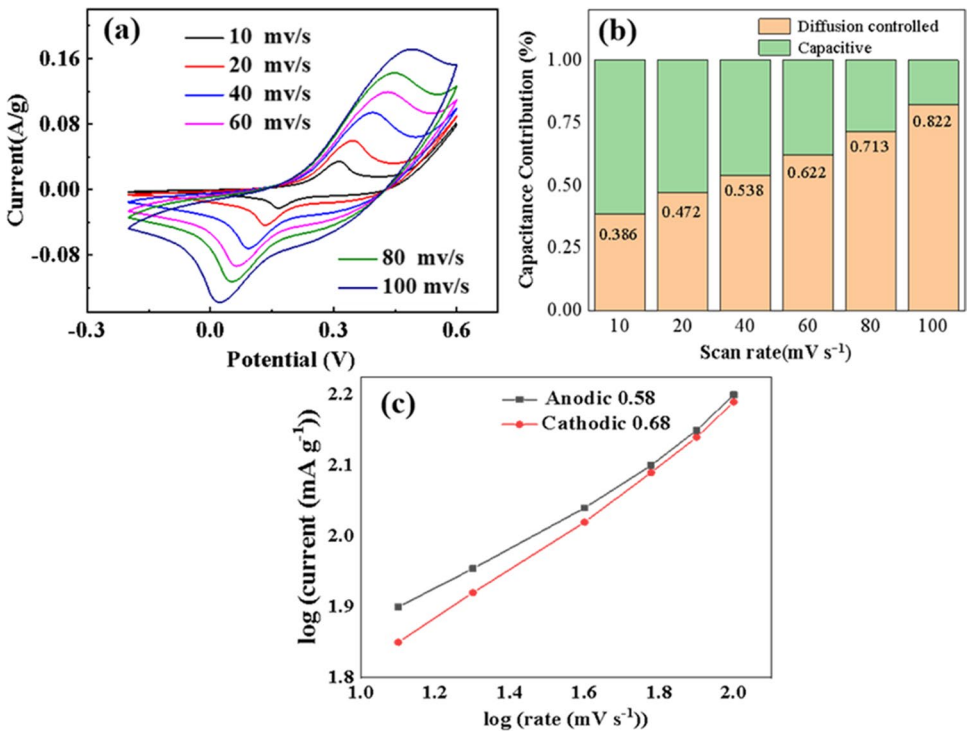

Fig. 5 **a** CV curves of $ZnCo_2O_4$ NWAs at the scan rate from 10 to 100 mV $s.^{-1}$. **b** Contribution rate of pseudocapacitance at different sweeping speeds. **c** Linear diagram of log (i) and log (v)

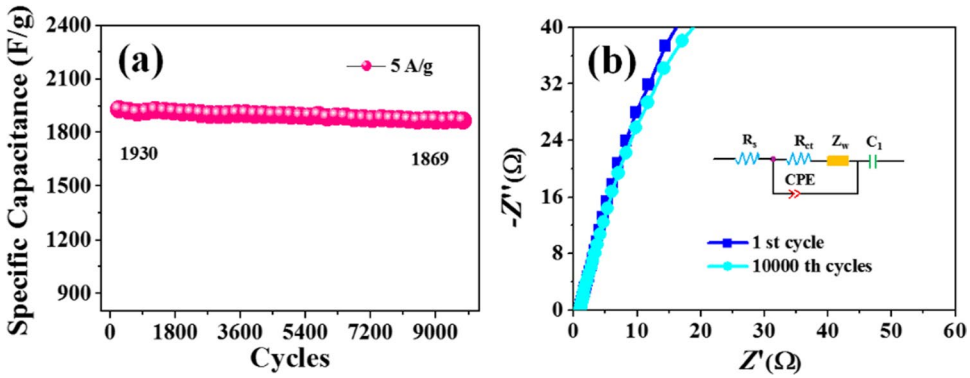

Fig. 6 **a** 10,000 cycles of stability test at current density 5 A g^{-1}; **b** Nyquist diagrams of the first and 10,000th cycles of $ZnCo_2O_4$ nanostructures are illustrated as equivalent circuit diagrams

Table 1 Comparison of properties of electrode materials with references

Electrode material	Current density (A g^{-1})	Specific capacity (F g^{-1})	Cycle times	Capacitance retention (%)	Ref
$ZnCo_2O_4$ nanowires	1	1099	5000	84.82%	[41]
$ZnCo_2O_4$ nanosheets	2.5	1250	10,000	96.5%	[42]
$CoFe_2O_4$ hollow microsphere	20	1231	500	98%	[43]
$NiMoO_4$ nanosheets	1	1853	2500	65%	[44]
Porous $ZnCo_2O_4$	2	220.6	8000	67.5%	[45]
$NiMoO_4$/$CoMoO_4$ nanorods	1	1445	3000	78.8%	[46]
Co_3O_4@$NiMoO_4$	10	913.25	3000	88%	[47]
$ZnCo_2O_4$/MnO_2	10	1526	8000	94.5%	[48]
$ZnCo_2O_4$ nanotubes	1	770	3000	89.5%	[49]
$ZnCo_2O_4$ NWAs	1	2300	10,000	96.84%	This paper

indicate that $ZnCo_2O_4$ has superior electrochemical capability at high rates.

The cycling stability is also an important factor in evaluating the performance of the material. In the experiments, we tested the capacity retention of the material after 10,000 cycles. As shown in Fig. 6a, the specific capacitance of the $ZnCo_2O_4$ NWAs electrode decreased from 1930 F g^{-1} to 1869 F g^{-1} at a current density of 5 A g^{-1}, maintaining a capacitance retention of 96.84%. We have compared our research work with the electrochemical properties of other materials, as shown in Table 1. Figure 6b shows the impedance plots for the $ZnCo_2O_4$ NWAs electrode after the 1st and 10,000th cycles. There is no significant difference in the arc increment in the high-frequency region, indicating that this holds up well over the 10,000th cycle. After 10,000 cycles, the linear slope in the low-frequency region decreases, which indicates a slight increase in the diffusion resistance of the material, which is due to the corrosion of the nanomaterials by dissolved oxygen in the electrolyte, resulting in the loss of some active substances [40]. The extremely small impedance and excellent cycling stability of the material may be mainly attributed to the interweaving of nanowires, which creates a large surface area and thus improves the utilization of the electrode material.

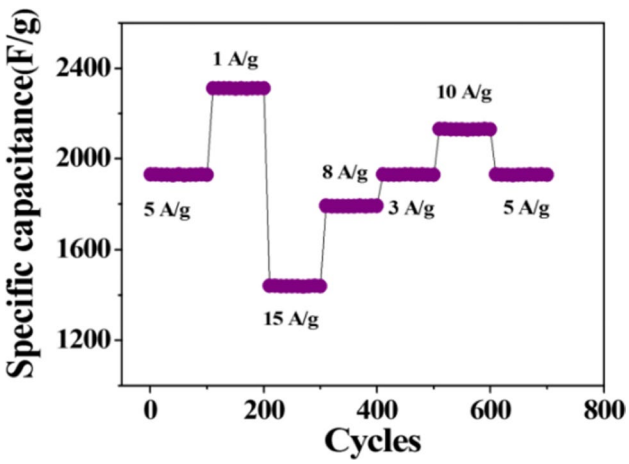

Fig. 7 Rate and cycle stability tests under different current densities

The rate performance of the $ZnCo_2O_4$ NWAs electrode at different current densities is shown in Fig. 7. At a current density of 5 A g^{-1}, the $ZnCo_2O_4$ NWAs electrode showed a stable specific capacity of 1947 F g^{-1} for the first 100 cycles. Over the next 600 cycles, varying the current density, the $ZnCo_2O_4$ NWAs electrode always showed a stable

capacitance. When returning to the initial current, its specific capacity was 1938 F g^{-1}. The specific capacity remained almost unchanged, indicating that the $ZnCo_2O_4$ NWAs electrode has excellent cycling stability performance. According to the above performance research, it is concluded that the reason why this material has these excellent properties is mainly due to the special structure of CC and NWAs. CC has better conductivity; the material grows directly on the conductive substrate and has better binding force with the material, which can effectively prevent the active material from falling off from the conductive substrate. This $ZnCo_2O_4$ NWAs structure is conducive to the transmission of electrolyte ions. Also, $ZnCo_2O_4$ NWAs grown on CC with nanostructures provide a relatively high specific surface area and abundant reactive active sites for the material, which improves the electrochemical reaction efficiency.

Synthesizing the above studies related to the performance, we conclude that the reasons for the excellent performance are as follows: firstly, the water bath method makes $ZnCo_2O_4$ grow uniformly on the conductive substrate, and the two have good bonding force. Then, after calcination treatment, the structure of the substrate is stabilized to eliminate the undesirable impurities generated in the early stage and ensure the uniform and stable dispersion of the metal on the carrier. Secondly, carbon cloth has the advantages of good electrical conductivity and large specific surface area. As the growth skeleton supporting the active material, the carbon cloth not only prevents the re-accumulation of $ZnCo_2O_4$ NWAs, but also enhances the connection between the carbon fiber skeleton and $ZnCo_2O_4$ NWAs, which constructs a high-speed channel for the charge transfer and storage. Finally, the special structure of nanowire arrays, which provides a very large specific surface area, shortens the diffusion distance of ions and improves the electrochemical properties of the material.

To further investigate the practical applications of the synthesized material, it was assembled into devices and its device performance was investigated. An asymmetric supercapacitor (ASC) device was assembled using $ZnCo_2O_4$ NWAs as the positive electrode and AC as the negative electrode. The device was tested in a two-electrode system with a 2 M KOH solution as the electrolyte.

Figure 8a shows the charging and discharging curves of the AC electrode at current densities of 1, 3, 5, 8, 10, and 15 A g^{-1}, respectively. The charging and discharging curves are nearly triangular with good symmetry, which indicates that the AC electrode has a good charge and discharge reversibility. The specific capacitance values of the AC electrode at different current densities were calculated according to Eq. 1, as shown in Fig. 8b. The specific capacitance of the device is 227, 208, 190, 181, 171, and 131 F g^{-1} with the current densities of 1, 3, 5, 8, 10, and 15 A g^{-1}, respectively. The materials were further assembled into $ZnCo_2O_4$//AC asymmetric devices and the capacitive performance of the asymmetric devices was investigated. Under the condition of scanning speed of 8 mV s^{-1} and 2 M KOH electrolyte, $ZnCo_2O_4$ and AC are the cyclic voltammetry curves of positive and negative electrodes, respectively, as shown in Fig. 9a. The voltage window of the device is different between the potential window of the positive and negative electrodes. The theoretical potential window of $ZnCo_2O_4$ NWAs//AC reaches 1.6 V. Figure 9b shows the CV curves of the $ZnCo_2O_4$ NWAs//AC device for different potential windows. It is clear that the shape of the CV curves at different voltage windows is broadly similar and the area increases with increasing potential window, which indicates that the device is stable over a potential window range of 0 to 1.6 V. It is consistent with the theoretical potential window. Figure 9c shows the CV curves of the ASC device at different scan rates. The overall shape of the CV curves hardly changes as the scan rates increase and the area of the curve increases with the scan rate. It indicated that the electrochemical reaction speeds up and the amount of charge stored increases with the increase of the scanning rates. Charge and discharge tests of the ACS devices were carried out at current densities of 1, 3, 5, 8, 10, and 15 A g^{-1}, as shown in Fig. 9d. The charge–discharge curves are basically symmetrical, indicating good electrochemical stability

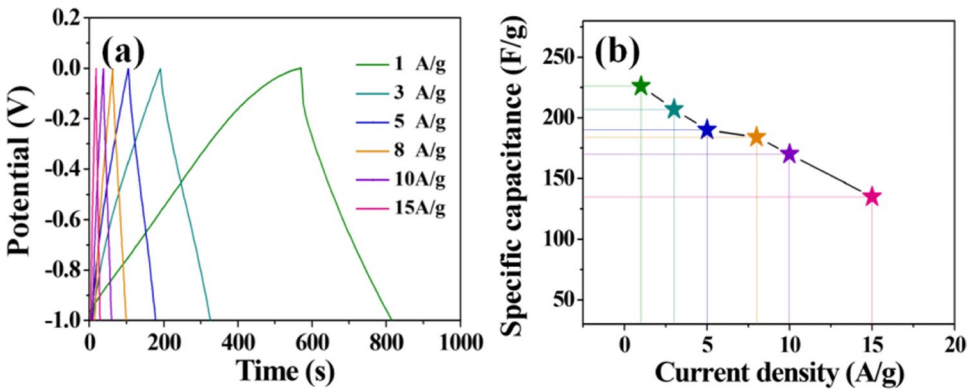

Fig. 8 **a** Charge and discharge tests of AC under different current intensities; **b** specific capacitance diagram of AC under different current densities

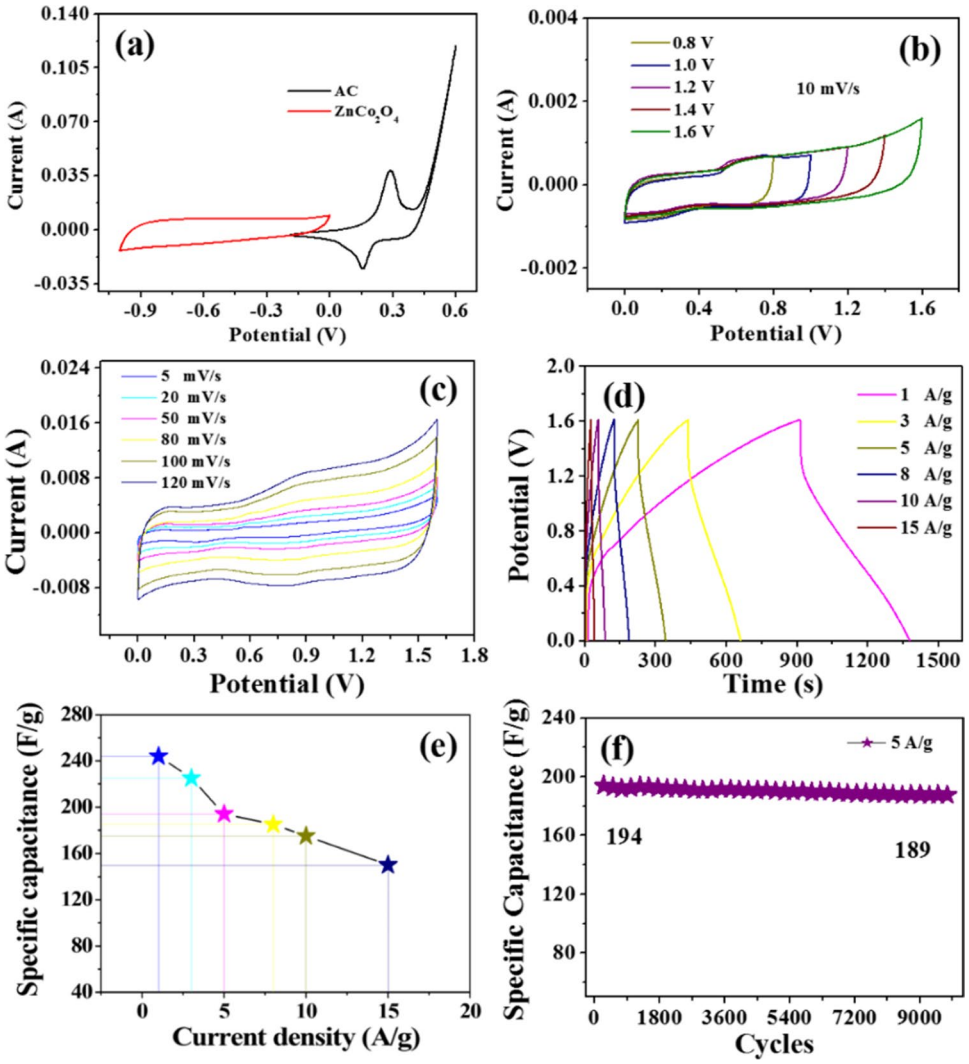

Fig. 9 **a** Cyclic voltammetry of $ZnCo_2O_4$ and AC electrode materials in the electrolyte with sweep speed of 8 mV s^{-1} and 2 M KOH under the condition of three electrodes; **b** cyclic voltammetry curve of $ZnCo_2O_4$// AC asymmetric device when the voltage window changes from 0.8 to 1.6 V at a sweep speed of 10 mV s^{-1}; **c** cyclic voltammetry test diagram of $ZnCo_2O_4$//AC asymmetric device at different sweep speeds; **d** charge–discharge curve test diagram of $ZnCo_2O_4$// AC at different current density; **e** specific capacitance diagram of $ZnCo_2O_4$//AC asymmetric devices at different current densities; **f** stability test diagram of $ZnCo_2O_4$//AC asymmetric device with 10,000 cycles at the current density of 5 A $g.^{-1}$

and performance. The specific capacitance of the device was calculated according to Eq. 1 and the results are shown in Fig. 9e. The specific capacitance of the device was 248, 222, 194, 184, 176, and 151 F g^{-1} at current densities of 1, 3, 5, 8, 10, and 15 A g^{-1}. The device was then tested for cycling stability, as shown in Fig. 9f. The device was charged and discharged for 10,000 cycles at a current density of 5 A g^{-1} and the specific capacitance value decreased from 194 F g^{-1} at the beginning to 189 F g^{-1} with a retention rate of 97.42%, showing excellent cycling stability.

Experimentally, the assembly of the device involves a mass relationship between the positive and negative active substances which we can calculate by means of the charge balance relationship: $q+ = q^-$ [50]. $q+$ and q^- represent the charge stored at the positive and negative electrodes respectively. The value of the charge q at each electrode is related to the specific capacity of the electrode material (C_s), the voltage of the discharge section of the electrode material (ΔV), and the mass of the electrode material, as shown in Eq. 2. Rectifying the equations, the equation for the relationship between the positive (m^+) and negative (m^-) electrode masses can be derived as follows: Eq. 3. Bringing in the relevant data respectively, the mass ratio of the positive and negative electrode materials for the asymmetric device is calculated as $m^+/m^- \approx 1/8$.

Finally, we tested the morphology and structure of the nanomaterials before and after cycling, as shown in Fig. 10a,b . From the figures, we can find that the structure of the materials before and after cycling is basically unchanged, and the linear structure is still well maintained. This indicates that the $ZnCo_2O_4$ NWAs nanomaterials prepared by this method have excellent structural stability. In order to observe the physicochemical properties of the materials after cycling, we also measured the XRD and XPS analyses, as shown in Fig. 10c,d. It can be seen from the figures that no significant changes were found in the $ZnCo_2O_4$ NWAs material after cycling, but there was a slight trend of weakening of the XRD or XPS characteristic peak intensity.

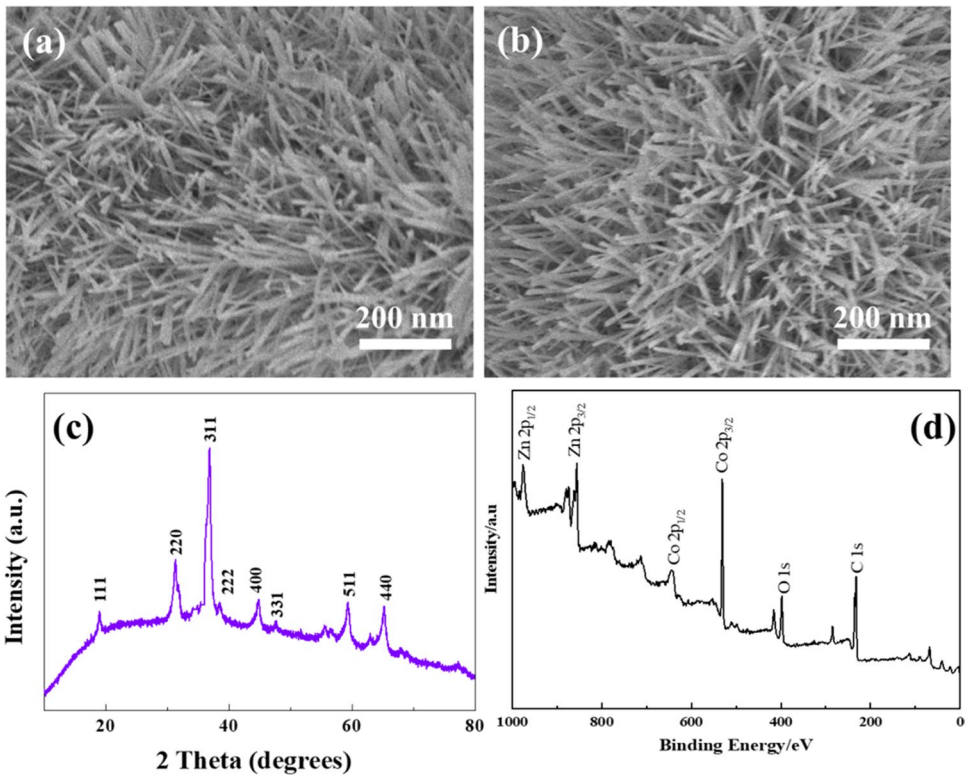

Fig. 10 SEM image of $ZnCo_2O_4$ NWAs: **a** cycle before; **b** after circulation; **c** XRD patterns of $ZnCo_2O_4$ NWAs materials after cycling; **d** XPS of $ZnCo_2O_4$ NWAs after cycling

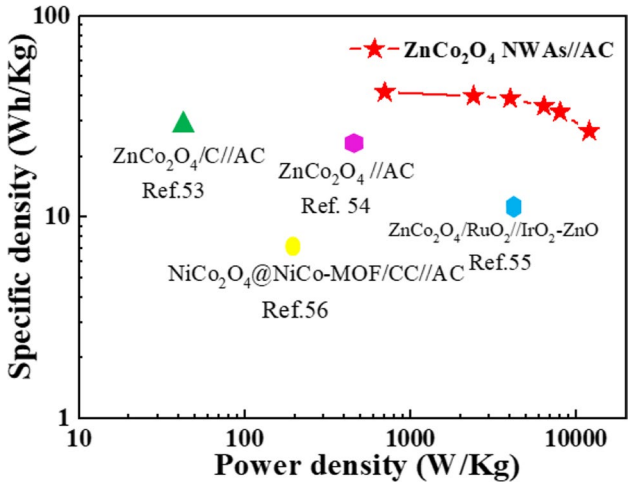

Fig. 11 Energy density and power density of $ZnCo_2O_4$ NWAs//AC compared to other energy storage devices

This indicates that the experimentally prepared $ZnCo_2O_4$ NWAs have good cycling stability [51, 52], which is consistent with the SEM test.

We compared our work with other energy storage devices [53–56], as shown in Fig. 11. The energy density and power density of the $ZnCo_2O_4$ NWAs//AC asymmetric device were calculated according to Eqs. 4 and 5, respectively. At an operating voltage of current density of 1 A g^{-1}, the maximum energy density is 88.18 Wh kg^{-1} and the corresponding power density is 800 W kg^{-1}. At a current density of 15 A g^{-1}, the device has a maximum power density of 12,000 W kg^{-1} and an energy density of 53.69 Wh kg^{-1}. The device we have assembled can be comparable to the lithium batteries.

Conclusion

In summary, a binary metal oxide $ZnCo_2O_4$ NWAs with excellent electrochemical performances were prepared by a pot water bath method and calcination treatment. The prepared $ZnCo_2O_4$ NWAs electrode achieved a high specific capacitance of 2300 F g^{-1} at a current density of 1 A g^{-1} and maintained an initial specific capacitance of 96.84% after 10,000 charge/discharge cycles at a current density of 5 A g^{-1}. The NWAs structure gives the $ZnCo_2O_4$ material a good specific capacitance and excellent cycling stability. In addition, we have assembled a $ZnCo_2O_4$ NWAs//AC asymmetric device. The $ZnCo_2O_4$ NWAs//AC asymmetric device with good specific capacity (248 F g^{-1} at 1 A g^{-1}) and excellent capacity retention rate (97.42% after 10,000 cycles at 5 A g^{-1}). The device has a maximum energy density of 88.18 Wh kg^{-1} (specific power 800 W kg^{-1}) and a maximum power density of 12,000 W kg^{-1} (specific energy 53.69 Wh kg^{-1}). All these results confirm that the prepared electrodes and devices are very promising for the development of energy storage devices.

Funding This research work was supported by the Young Scientific Research Item of Harbin University of Commerce (18XN034), the National Natural Science Foundation of China (No. 52002099), and the Foundation of State Key Laboratory of High-efficiency Utilization of Coal and Green Chemical Engineering (Grant No. 2022-K74).

Declarations

Competing interests The authors declare no competing interests.

References

1. Wang Y, Wu X, Han Y, Li T (2021) Flexible supercapacitor: overview and outlooks. J Energy Storage 52:441–473. https://doi.org/10.1016/j.est.2021.103053
2. Raza W, Ali F, Raza N, Luo Y, Kim KH, Yang J, Kumar S, Mehmood A, Kwon EE (2018) Recent advancements in supercapacitor technology. Nano Energy 52:441–473. https://doi.org/10.1016/j.nanoen.2018.08.013
3. Najib S, Erdem E (2019) Current progress achieved in novel materials for supercapacitor electrodes: mini review. Nanoscale Adv 1:2817–2827. https://doi.org/10.1039/c9na00345b
4. Meng Q, Cai K, Chen Y, Chen L (2017) Research progress on conducting polymer based supercapacitor electrode materials. Nano Energy 36:268–285. https://doi.org/10.1016/j.nanoen.2017.04.040
5. Chen GZ (2016) Supercapacitor and supercapattery as emerging electrochemical energy stores. Int Mater Rev 62:173–202. https://doi.org/10.1080/09506608.2016.1240914
6. Ren B, Fan M, Zhang B, Wang J (2018) Novel hollow NiO@Co_3O_4 nanofibers for high-performance supercapacitors. J Nanosci Nanotechnol 18:7004–7010. https://doi.org/10.1166/jnn.2018.15451
7. Chen PC, Hsieh SJ, Zou J, Chen CC (2014) Selectively dealloyed Ti/TiO_2 network nanostructures for supercapacitor application. Mater Lett 133:175–178. https://doi.org/10.1016/j.matlet.2014.06.165
8. Li K, Liu X, Zheng T, Jiang D, Zhou Z, Liu C, Zhang X, Zhang Y, Losic D (2019) Tuning MnO_2 to FeOOH replicas with biotemplate 3D morphology as electrodes for high performance asymmetric supercapacitors. Chem Eng J 370:136–147. https://doi.org/10.1016/j.cej.2019.03.190
9. Wei W, Chen Z, Zhang Y, Chen J, Wan L, Du C, Xie M, Guo X (2020) Full-faradaic-active nitrogen species doping enables high-energy-density carbon-based supercapacitor. J Energy Chem 48:277–284. https://doi.org/10.1016/j.jechem.2020.02.011
10. Shen C, Wang X, Li S, Wang JG, Zhang W, Kang F (2013) A high-energy-density micro supercapacitor of asymmetric MnO_2–carbon configuration by using micro-fabrication technologies. J Power Sources 234:302–309. https://doi.org/10.1016/j.jpowsour.2012.10.101
11. Guo Y, Wang T, Chen X, Wu D (2021) Agar-based porous electrode and electrolyte for flexible symmetric supercapacitors with ultrahigh energy density. J Power Sources 507:230252. https://doi.org/10.1016/j.jpowsour.2021.230252
12. Wu Z, Pu X, Ji X, Zhu Y, Jing M, Chen Q, Jiao F (2015) High energy density asymmetric supercapacitors from mesoporous $NiCo_2S_4$ nanosheets. Electrochim Acta 174:238–245. https://doi.org/10.1016/j.electacta.2015.06.011
13. Choudhary N, Li C, Moore J, Nagaiah N, Zhai L, Jung Y, Thomas J (2017) Asymmetric supercapacitor electrodes and devices. Adv Mater 29:1605336. https://doi.org/10.1002/adma.201605336
14. Balaji TE, Tanaya DH, Maiyalagan T (2021) Recent trends in bimetallic oxides and their composites as electrode materials for supercapacitor applications. Chem Electro Chem 8:1723–1746. https://doi.org/10.1002/celc.202100098
15. Raza N, Kumar T, Singh V, Kim KH (2021) Recent advances in bimetallic metal-organic framework as a potential candidate for supercapacitor electrode material. Coordin Chem Rev 430:213660. https://doi.org/10.1016/j.ccr.2020.213660
16. An C, Zhang Y, Guo H, Wang Y (2019) Metal oxide-based supercapacitors: progress and prospectives. Nanoscale Adv 1:4644–4658. https://doi.org/10.1039/c9na00543a
17. Wang Z, Jia W, Jiang M, Chen C, Li Y (2016) One-step accurate synthesis of shell controllable $CoFe_2O_4$ hollow microspheres as high-performance electrode materials in supercapacitor. Nano Res 9:2026–2033. https://doi.org/10.1007/s12274-016-1093-y
18. Han Y, Jiao Y, Lv G, Pang Y, Zhou J, Xue Z, Li L, Song L, Liu Y (2020) High-performance strontium and bismuth bimetallic oxides electrode: combine first-principles calculations with electrochemical tests. Mater Today Commun 24:100927. https://doi.org/10.1016/j.mtcomm.2020.100927
19. Guan C, Liu X, Ren W, Li X, Cheng C, Wang J (2017) Rational design of metal-organic framework derived hollow $NiCo_2O_4$ arrays for flexible supercapacitor and electrocatalysis. Adv Energy Mater 7:1602391. https://doi.org/10.1002/aenm.201602391
20. Liu B, Liu B, Wang Q, Wang X, Xiang Q, Chen D, Shen G (2013) New energy storage option: toward $ZnCo_2O_4$ nanorods/nickel foam architectures for high-performance supercapacitors. ACS Appl Mater Inter 5:10011–10017. https://doi.org/10.1021/am402339d
21. Zhu J, Song D, Pu T, Li J, Huang B, Wang W, Zhao C, Xie L, Chen L (2018) Two-dimensional porous $ZnCo_2O_4$ thin sheets assembled by 3D nanoflake array with enhanced performance for aqueous asymmetric supercapacitor. Chem Eng J 336:679–689. https://doi.org/10.1016/j.cej.2017.12.035
22. Shang Y, Xie T, Ma C, Su L, Gai Y, Liu J, Gong L (2018) Synthesis of hollow $ZnCo_2O_4$ microspheres with enhanced electrochemical performance for asymmetric supercapacitor. Electrochim Acta 286:103–113. https://doi.org/10.1016/j.electacta.2018.08.025
23. Xu L, Zhao Y, Lian J, Xu Y, Bao J, Qiu J, Xu L, Xu H, Hua M, Li H (2017) Morphology controlled preparation of $ZnCo_2O_4$ nanostructures for asymmetric supercapacitor with ultrahigh energy density. Energy 123:296–304. https://doi.org/10.1016/j.energy.2017.02.018
24. Wang X, Lim TT (2010) Solvothermal synthesis of C-N codoped TiO_2 and photocatalytic evaluation for bisphenol A degradation using a visible-light irradiated LED photoreactor. Appl Catal B-Environ 100(1–2):355–364. https://doi.org/10.1016/j.apcatb.2010.08.012
25. Chen F, Luo H, Cheng Y, Liu J, Wang X, Gong R (2019) Fe/Fe_3O_4@ N-doped carbon hexagonal plates decorated with Ag nanoparticles for microwave absorption. ACS Appl Nano Mater 2(11):7266–7278. https://doi.org/10.1021/acsanm.9b01755
26. Kayaci F, Ozgit-Akgun C, Donmez I, Biyikli N, Uyar T (2012) Polymer–inorganic core–shell nanofibers by electrospinning and atomic layer deposition: flexible nylon–ZnO core–shell nanofiber mats and their photocatalytic activity. ACS Appl Mater Inter 4(11):6185–6194. https://doi.org/10.1021/am3017976
27. Huang G, Xu S, Liu Z, Yuan S, Zhang C, Ai J, Li X (2020) Ultrafine cobalt-doped iron disulfide nanoparticles in ordered mesoporous carbon for efficient hydrogen evolution. Chem Cat Chem 12(3):788–794. https://doi.org/10.1002/cctc.201901759
28. Padalkar NS, Sadavar SV, Shinde RB, Patil AS, Patil UM, Magdum VV, Gunjakar JL (2022) 2D–2D nanohybrids of Ni-Cr-layered double hydroxide and graphene oxide nanosheets: electrode for hybrid asymmetric supercapacitors. Electrochim Acta 424:140615. https://doi.org/10.1016/j.electacta.2022.140615

29. Zikirina A, Kadyrzhanov KK, Kenzhina IE, Kozlovskiy AL, Zdorovets MV (2021) Study of defect formation processes under heavy ion irradiation of $ZnCo_2O_4$ nanowires. Opt Mater 118:111282. https://doi.org/10.1016/j.optmat.2021.111282
30. Wang J, Wang G, Wang S, Hao J, Liu B (2022) Preparation of $ZnCo_2O_4$ Nanosheets Coated on evenly arranged and fully separated Nanowires with high capacitive and photocatalytic properties by a one-step low-temperature water bath method. ChemistrySelect 7(13):e202200472. https://doi.org/10.1002/slct.202200472
31. Yan L, Zhu C, Hao J, Liang X, Bai Y, Hu Q, Xiang B (2021) A universal voltage design for triggering manganese dioxide defects construction to significantly boost the pseudocapacitance. Adv Funct Mater 31(30):2102693. https://doi.org/10.1002/adfm.202102693
32. Tiwari N, Kadam S, Kulkarni S (2021) Synthesis and characterization of $ZnCo_2O_4$ electrode for high-performance supercapacitor application. Mater Lett 298:130039. https://doi.org/10.1016/j.matlet.2021.130039
33. Bhagwan J, Hussain SK, Yu JS (2020) Aqueous asymmetric supercapacitors based on $ZnCo_2O_4$ nanoparticles via facile combustion method. J Alloy Compd 815:152456. https://doi.org/10.1016/j.jallcom.2019.152456
34. Yuan L, Liu Y, Xin N, He R (2022) Hierarchical structure $ZnCo_2O_4$/$ZnCo_2O_4$/CoO@ rGO/GO as cathode material to construct high energy density supercapacitor. J Energy Storage 52:104727. https://doi.org/10.1016/j.est.2022.104727
35. Chen H, Wang J, Han X, Liao F, Zhang Y, Gao L, Xu C (2019) Facile synthesis of mesoporous $ZnCo_2O_4$ hierarchical microspheres and their excellent supercapacitor performance. Ceram Int 45(7):8577–8584. https://doi.org/10.1016/j.ceramint.2019.01.176
36. Xiong S, Lin M, Wang L, Liu S, Weng S, Jiang S, Chen J (2021) Defects-type three-dimensional Co_3O_4 nanomaterials for energy conversion and low temperature energy storage. Appl Surf Sci 546:149064. https://doi.org/10.1016/j.apsusc.2021.149064
37. Liu Y, Wu X (2021) Hydrogen and sodium ions co-intercalated vanadium dioxide electrode materials with enhanced zinc ion storage capacity. Nano Energy 86:106124. https://doi.org/10.1016/j.nanoen.2021.106124
38. Lin M, Shao F, Tang Y, Lin H, Xu Y, Jiao Y, Chen J (2022) Layered Co doped MnO_2 with abundant oxygen defects to boost aqueous zinc-ion storage. J Colloid Interf Sci 611:662–669. https://doi.org/10.1016/j.jcis.2021.12.136
39. Tang Y, Wu L, Wei W, Wen D, Guo Q, Liang W, Xiao L (2018) Study of the thermal properties during the cyclic process of lithium ion power batteries using the electrochemical-thermal coupling model. Appl Therm Eng 137:11–22. https://doi.org/10.1016/j.applthermaleng.2018.03.067
40. Yin L, Gao YJ, Jeon I, Yang H, Kim JP, Jeong SY, Cho CR (2019) Rice-panicle-like γ-Fe_2O_3@C nanofibers as high-rate anodes for superior lithium-ion batteries. Chem Eng J 356:60–68. https://doi.org/10.1016/j.cej.2018.09.017
41. Keshmiri N, Najmi P, Ramezanzadeh B, Ramezanzadeh M, Bahlakeh G (2021) Nano-scale P, Zn-codoped reduced-graphene oxide incorporated epoxy composite; synthesis, electronic-level DFT-D modeling, and anti-corrosion properties. Prog Org Coat 159:106416. https://doi.org/10.1016/j.porgcoat.2021.106416
42. Rajesh JA, Ahn KS (2021) Facile hydrothermal synthesis and supercapacitor performance of mesoporous necklace-type $ZnCo_2O_4$ nanowires. Catalysts 11:1516. https://doi.org/10.3390/catal11121516
43. Javed MS, Hussain I, Batool S, Siyal SH, Najam T, Shah SSA, Imran M, Assiri MA, Hussain S (2021) Energy storage properties of hydrothermally processed ultrathin 2D binder-free $ZnCo_2O_4$ nanosheets. Nanotechnology 32(38):385402. https://doi.org/10.1088/1361-6528/ac0c42
44. Qing C, Yang C, Chen M, Li W, Wang S, Tang Y (2018) Design of oxygen-deficient $NiMoO_4$ nanoflake and nanorod arrays with enhanced supercapacitive performance. Chem Eng J 354:182–190. https://doi.org/10.1016/j.cej.2018.08.005
45. Zhang D, Zhang Y, Li X, Luo Y, Huang H, wang J, Chu PK, (2016) Self-assembly of mesoporous $ZnCo_2O_4$ nanomaterials: density functional theory calculation and flexible all-solid-state energy storage. J Mater Chem A 4:568–577. https://doi.org/10.1039/c5ta07105d
46. Nti F, Anang DA, Han JI (2018) Facilely synthesized $NiMoO_4$/$CoMoO_4$ nanorods as electrode material for high performance supercapacitor. J Alloy Compd 742:342–350. https://doi.org/10.1016/j.jallcom.2018.01.289
47. Dong T, Li M, Wang P, Yang P (2018) Synthesis of hierarchical tube-like yolk-shell Co_3O_4@$NiMoO_4$ for enhanced supercapacitor performance. Int J Hydrogen Energ 43:14569–14577. https://doi.org/10.1016/j.ijhydene.2018.06.067
48. Reece R, Lekakou C, Smith PA (2020) A high-performance structural supercapacitor. ACS Appl Mater Inter 12:25683–25692. https://doi.org/10.1021/acsami.9b23427
49. Peixoto LC, Bortolozo AD, Garcia A, Osório WR (2016) Performance of new Pb-Bi alloys for Pb-acid battery applications: EIS and polarization study. J Mater Eng Perform 25:2211–2221. https://doi.org/10.1007/s11665-016-2059-7
50. Wang H, Zhu C, Chao D, Yan Q, Fan HJ (2017) Nonaqueous hybrid lithium-ion and sodium-ion capacitors. Adv Mater 29(46):1702093. https://doi.org/10.1002/adma.201702093
51. Tan B, Fang Y, Chen Q, Ao X, Cao Y (2020) Preparation of a $CaFe_2O_4$/$ZnCo_2O_4$ composite material and its photocatalytic degradation of tetracycline. Opt Mater 109:110470. https://doi.org/10.1016/j.optmat.2020.110470
52. Li G, Zhang W, Hou J, Li T, Li P, Wang Y, Wang K (2020) Enhanced visible light photochemical activity and stability of MoS_2/Cu_2O nanocomposites by tunable heterojunction. Mater Today Commun 23:100933. https://doi.org/10.1016/j.mtcomm.2020.100933
53. Lu Y, Wang L, Chen M, Wu Y, Liu G, Qi P, Tang Y (2021) Rationally designed hierarchical $ZnCo_2O_4$/C core-shell nanowire arrays for high performance and stable supercapacitors. J Alloy Compd 876:160037. https://doi.org/10.1016/j.jallcom.2021.160037
54. Xiang K, Wu D, Fan Y, You W, Zhang D, Luo JL, Fu XZ (2021) Enhancing bifunctional electrodes of oxygen vacancy abundant $ZnCo_2O_4$ nanosheets for supercapacitor and oxygen evolution. Chem Eng J 425:130583. https://doi.org/10.1016/j.cej.2021.130583
55. Wang J, Ye T, Shao Y, Lu Z, Lin Y, Wu H, Tang D (2021) Flower-like nanostructured $ZnCo_2O_4$/RuO_2 electrode materials for high performance asymmetric supercapacitors. J Electrochem Soc 168(12):120553. https://doi.org/10.1149/1945-7111/ac42a4
56. Lu J, Wang J, Gong J, Hu C (2022) Design of flower-shaped array of nickel-cobalt nanosheets for high-performance asymmetric supercapacitors. J Mater Sci-Mater El 33(23):18922–18937. https://doi.org/10.1007/s10854-022-08768-8